Research Article

Properties of synthetic graphite from boric acid-added pitch: performance as anode in lithium-ion batteries

Jin Ung Hwang[1,2] · Won Jun Ahn[1] · Ji Sun Im[1,3] · Jong Dae Lee[2]

© The Author(s) 2021   OPEN

Abstract

Synthetic graphite is produced by a heat treatment process using a carbon precursor (pitch, coke), but it is difficult to produce synthetic graphite of high quality due to the high-temperature process (minimum 3000 °C). Elements used as additive to lower temperature the graphitic process include boron, phosphorus, and nitrogen. Boron is known as a graphitization additive, because it accelerates the homogeneous continuous graphitization process of the entire carbon without any formation of specific carbon components such as graphite. In this study, various amounts of boron and PFO (pyrolysis fuel oil, carbon precursor) were used in an attempt to reveal the boron additive effect. Pitch was produced using a boric acid and pyrolysis fuel oil (PFO), and high-temperature carbonization was carried out at 2600 °C. As a result, synthetic graphite exhibiting high crystallinity at a relatively low temperature was produced. The electrochemical performance of several boron-doped and non-doped carbon materials with different structures as anodes in lithium-ion batteries was investigated by a structure analysis.

Keywords Pitch · Boric acid · Synthetic graphite · Anode · Lithium-ion battery

1 Introduction

Graphite used as an anode electrode material for lithium-ion batteries (LIBs) is largely classified into natural graphite (NG) and synthetic graphite (SG). NG is obtained in the form of flakes with a large aspect ratio by the purification process. In order to use flake-shaped NG as a anode material, a spheroidization process must be performed. However, this process results in pores and surface defects on the anode materials. Due to these structural defects, natural graphite can storage more lithium ions than the theoretical capacity of graphite (LiC_6, 372 mAh/g). SG, on the other hand, is manufactured from a carbon precursor (pitch, cokes etc.), and it can maintain its quality and its performance can be controlled by changing the manufacturing process. In order to produce high-quality synthetic graphite for anode materials, however, a high temperature of 3000 °C or higher is required [1–3].

During the manufacturing process of SG, the structure of the carbon precursor depends on the manufacturing temperature. The characteristics of an amorphous structure arise when the manufacturing temperature of the carbon materials is ~ 1200 °C. Amorphous carbon (called soft carbon) exhibits a disordered structure and has many pores and defects. These pores and defects can serve as lithium ion storage, thus offering high capacity and speed performance, but they cause low stability. In addition, the crystallinity is increased by 2400–2700 °C and the crystals

are rearranged at subsequently higher temperature. It was reported that the carbon material (not SG) produced at the above heat treatment temperature exhibited a capacity of 240–300 mAh/g [4, 5]. Finally, a graphitic structure is obtained at a temperature of 3000 °C or higher, where a layered structure stacked many times with each layer connected via van der Waals force is formed. The structure shows excellent electrical conductivity and structural stability. However, it is difficult to manufacture good quality SG because high processing temperature is required [6–11].

Several strategies have been studied to manufacture SG, such as graphitizing with a metal-based additive. In general, the metal-based additives for manufacturing SG are boron, magnesium, aluminum, calcium, etc. Among them, boron component materials (boric acid (H_3BO_3), trioxide (B_2O_3), etc.) have been studied as graphitization accelerated metal additive. H_3BO_3 provides protons as Brønsted acids to help produce aromatic hydrocarbons. However, an excess H_3BO_3 can cause rapid thermal condensation reaction (such as coking reaction), during the pitch manufacturing process. And, H_3BO_3 is decomposed into HBO_2 and B_2O_3 at pitch synthesis temperature (400 °C). B_2O_3 is reacted with carbon to produce B_4C during graphitization process. And B_4C particles can be act as diffusion point for boron to improve the crystallinity of the produced graphite [10–23]. Yim et al. researched the effects of boron doping on the structure and performance of pyrolytic carbon from resins (hard carbon) with higher intercalation capacity [24]. Tojo et al. reported that boron doping of graphite-based pitch coke was effective in terms of the enhancing the electrochemical performance [25].

In this study, the boron added effect according to the petroleum residue [pyrolysis fuel oil (PFO) and boric acid ratio] in the feedstock was studied and produced pitch to improve the characteristic properties for SG. The manufactured pitch was thermal treated at lower graphitization temperature (2500 °C). Boron-doped graphite was characterized to investigate the effect of boron doping used boric acid. Emphasis was placed on the following two aspects: (1) the influence of boric acid and content on the development of the pitch's properties and (2) the relationship between the structure characteristics and the amount of boron compound in the substitution position in the carbon lattice and the anodic behavior of the SG. The intercalation spacing, d002, and crystal structures along the c axis, Lc, and a axis, La, calculated from X-ray diffraction (XRD) are used in the study to assess the graphitization ratio of SG. In addition, electrochemical properties were investigated using a lithium-ion battery system. The pitch-based graphite with added boric acid was measured at a high graphitization ratio of up to 97.2%, which improved the initial efficiency and C-rate performance. The change

of structural properties by the addition of boric acid and the effect of the boron–carbon reaction by-product boron carbide (B_4C) on the electrochemical properties were discussed.

2 Experimental

2.1 Boron-added pitch and boron-doped SG preparation

We investigated the characteristics of the carbon precursor (pitch) derived SG according to the amount of boric acid and investigated the electrochemical properties by preparing SG using PFO as a raw material. Figure 1 shows a schematic diagram of this experiment. The carbon precursor was produced using a pitch obtained by reacting petroleum residue [LG Chemical CO., produced by NCC (Naphtha Cracking Center, South Korea)], and boric acid (H_3BO_3, Samchun chemical, 99.5%) was generated in a domestic refinery in a 1 L batch-type autoclave under atmospheric conditions with a N_2 flow at a reforming temperature of 420 °C for 3 h. Before the pitch manufacturing process, boric acid (0–7 wt%) was added to PFO. The synthesized pitch was called 4203-BX (X = 0, 1, 3, 5, 7) according to the amount of boric acid added. Also, the synthesized pitch was heat treated at 900 and 2500 °C to prepare SG. The SG was then crushed and classified (< 25 μm) for use as anode materials. These anode materials are called 4203-BX-2500 (X = 0, 1, 3, 5, 7). CMC (carboxymethyl cellulose, MTI Korea) and SBR (styrene-butadiene rubber, MTI Korea) were used as binder materials for the manufactured battery electrode.

2.2 Characterization of boron-added pitch

The softening point of the produced pitch was measured using a softening point analyzer (DP-70, Mettler Toledo) according to ASTM D3416. The heating rate was 4 °C/min in an N_2 atmosphere. The quinoline insoluble (Q.I.) fraction of the produced pitch was separated using quinoline solvent according to ASTM D4746. An elemental analysis was conducted to confirm the C, H, N, and S contents and the C/H ratio of the feedstock and the produced pitches using a Thermo Scientific FLASH EA-2000 Organic Elemental Analyzer.

2.3 Characterization of the SG

The X-ray diffraction (XRD, Rigaku D/Max 2200 V, Bruker: CuKα radiation) was used to measure the Bragg reflection from 4203-BX-2500, and the lattice parameters Lc and La of the samples were determined from the width of the

Fig. 1 Schematic diagram of the synthesis process for PFO-based 4203-BX-2500
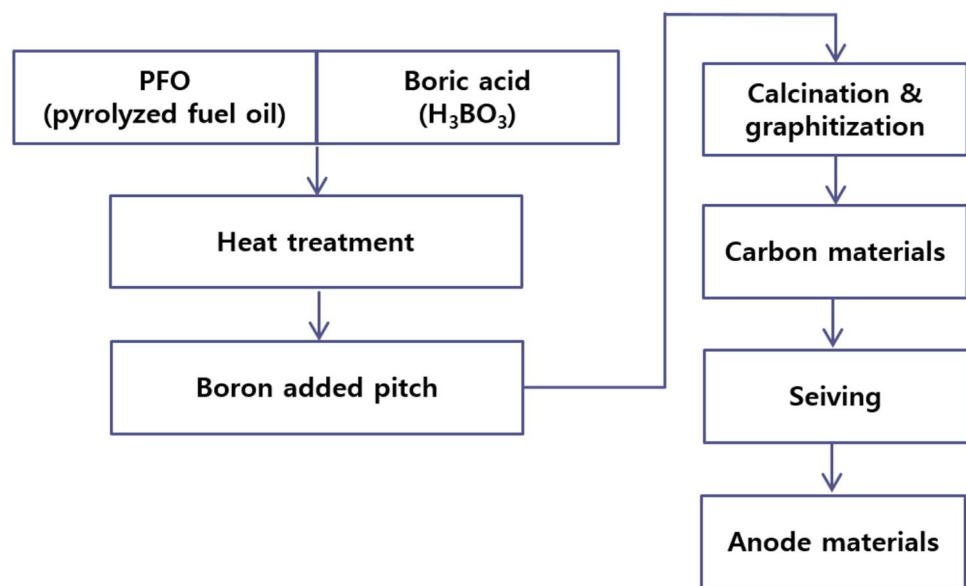
(002) and (110) planes. The samples were scanned in a 2θ range of 2°–80° with a step size of 0.02°.

Raman spectra of the 4203-BX-2500 samples were observed from 80 to 4300 cm^{-1} on a Laser Micro-Raman spectroscope (FRA 106/S, Bruker, Germany) using 532 nm He–Ne laser excitation. The doping type (B, C, O) in the 4203-BX-2500 was evaluated using X-ray photoelectron spectroscopy (XPS, KRATOS AXIS NOVA, Bruker: Al Kα radiation).

2.4 Cell preparation and electrochemical measurement

In order to confirm the electrochemical characteristics of the 4203-BX-2500 produced, Li metal was used as a counter electrode, and coin-type half cells were manufactured. The electrodes were prepared using a composition of 97 wt% of carbon active materials, 1.5 wt% of SBR, and 1.5 wt% of CMC, while dendritic cupper foil (thickness: 11 μm, Wellcos Co., Republic of Korea) was utilized as the current collector for the working electrode. First, the CMC and SBR were dissolved in deionized water, resulting in 1.5 wt% and 50 wt% solutions. After this step, the active materials and the binder were mixed according to the weight ratio, and the slurry was prepared by mixing at 2000 rpm for 30 s and at 2200 rpm for 30 s using a Thinky mixer (ARE-310, Thinky Co., Japan). The electrode slurry was cast on a Cu current collector by a doctor blade technique (240 μm), resulting in electrodes. The electrodes were initially dried for 12 h at room temperature and then further dried under reduced pressure of at least 10 mbar for 12 h at 120 °C. The electrode density of the dried electrodes was adjusted by roll pressing to 1.6 g/cm^3. They

were then cut to 12 mm diameter to produce coin-type electrodes. Lithium foil was used as the counter electrode in the coin-type cells for the electrochemical test. The electrolyte was a 1 M $LiPF_6$ solution in a mixture of ethylene carbonate (EC) and diethyl carbonate (DEC) (1:1 vol%. Wellcos Co., Republic of Korea). In addition, to evaluate the electrochemical characteristics of the fabricated half-cells, charge/discharge and C-rate characteristic tests were carried out using a WBCS 3000 battery cycler (Won A Tech, Republic of Korea). The charge–discharge and C-rate tests were carried out in the constant current–constant voltage (CC–CV) mode, the cut-off voltage was set to range from 0.01 to 1.5 V, and the speed characteristics were tested at different C-rates of 0.1 C, 0.5 C, 1 C, 2 C, and re-0.1 C. The 1 C-rate was set based on the theoretical capacity of graphite (372 mAh/g).

3 Results and discussion

3.1 Pitch characteristics according to the amount of added boric acid

The S.P. (softening point) and Q.I. (quinolone insoluble) of pitch were measured as listed in Table 1. It can be seen that S.P. increases with the addition of a small amount of boric acid (4203-B1) but decreases thereafter and Q.I. increases. In generally, H_3BO_3 is a Brønsted acid and can provide protons through successive ionization steps in the thermal condensation process. These protons can produce protonated complexes of aromatic hydrocarbons. Usually, the above reaction causes an increase in molecular weight and S.P [15]. However, if the boric acid is excessively added, the

reaction proceeds to cause rapidly thermal condensation reaction and coking, resulting in an increase in Q.I. It is considered that the average molecular weight of the pitch was lowered due to the coking of high molecular weight matter [16].

Table 2 shows the step yield and total yield for the process steps. The yield was reduced by boric acid at step 1. It is considered that, as described in Table 1, the low yield of pitch was produced by the rapid coking reaction by the addition of boric acid. Also, in step 2 and step 3, the yield decreases due to added boric acid. In particular, when boric acid was not added in step 3 the yield was 99%; when boric acid was added, however, the weight reduction was remarkable. According to Rocha's

study, the boron compound (B_2O_3) will react with carbon at temperatures between 2200 and 2500 °C. The reaction is shown in the following formula (1) [26]:

$$2B_2O_3(s) + 7C(s) = B_4C(s) + 6CO(g) \qquad (1)$$
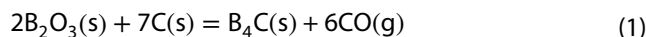
By the reaction given as formula (1), CO is finally formed with the by-product boron carbide (B_4C), and CO is removed as gas. Therefore, it is determined that a sharp decrease in yield occurred in step 3.

An elemental analysis was conducted to identify the C, H, O, N, and S contents and the H/C and O/C ratios, which are listed in Table 3. The addition of boric acid increases the O/C ratio. This is likely due to the increase in the amount of added boric acid (H_3BO_3). Boric acid

Table 1 Experimental conditions for thermal condensation of PFO

Sample name	Reaction condition						
	Temp. (°C)	Time (h)	H_3BO_3 (wt%)	N_2 flow (cc/min)	S.P (°C)[a]	Q.I (%)[b]
4203-B0	420	3	0	200	182.6	5.705
4203-B1	420	3	1	200	195.5	11.525
4203-B3	420	3	3	200	174.3	12.69
4203-B5	420	3	5	200	153.8	18.735
4203-B7	420	3	7	200	172.1	26.135

[a]Softening point

[b]Quinolone insoluble

Table 2 Coking yield of each heat treatment process

Amount of boric acid (wt%)	PFO → Pitch yield[a] (%)	Pitch → Coke yield[b] (%)	Coke → Graphite yield[c] (%)	Total yield[d] (%)
0	26.3	70.2	99.3	18.33
1	11.2	68.5	79.4	6.09
3	11	77.8	83.5	7.15
5	14	61.6	75.1	6.48
7	14.2	72.7	65.9	6.80

[a]Step 1, 420 °C, 3 h, N_2 atmosphere

[b]Step 2, 900 °C, 1 h, N_2 atmosphere

[c]Step 3, 2500 °C, 3 h, vacuum atmosphere

[d]PFO → graphite yield

Table 3 Elemental analysis of boric acid-added pitches

Sample name	C (%)	H (%)	O (%)	N (%)	S (%)	Diff[a] (%)	H/C ratio	O/C ratio
4203-B0	94.15	5.25	0.04	0	0	0.56	0.664	0.00032
4203-B1	93.03	4.96	0.12	0	0	1.89	0.635	0.00097
4203-B3	86.73	4.75	0.23	0	0	8.29	0.653	0.00199
4203-B5	85.72	4.55	0.3	0	0	9.43	0.632	0.00263
4203-B7	84.26	4.49	0.37	0	0	10.88	0.635	0.00330

[a]We regard the difference value between carbon, hydrogen, oxide, nitrene, and sulfur as the boron substituted weight (%) in the samples

undergoes two thermal decomposition processes at temperatures below 400 °C [27]:

$$H_3BO_3(s) \rightarrow HBO_2(s) + H_2O(g) \tag{2}$$

$$2HBO_2(s) \rightarrow B_2O_3(s) + H_2O(g) \tag{3}$$
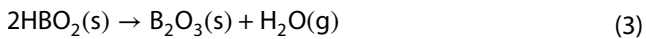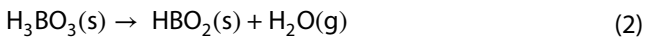
After the reactions delineated in (2) and (3), B_2O_3 was finally produced, which was analyzed to determine the amount of O element.

3.2 Properties of carbon materials produced from boric acid-added pitch

Figure 2 shows the SEM image of 4203-BX-2500 (X = 0, 1, 3, 5, 7). The prepared sample shows a flack shape by crush process. The high-resolution image was inserted to observe the surface morphology in detail. The surface of 4203-BX-2500 was not changed by regardless of the boron content. Therefore, it is expected that there is no difference in electrochemical properties based on the shape of anode material.

Figure 3, 4 and Table 4, respectively, show XRD graph, mechanism of boron transfer by crystalline B_4C and the calculated L_a, L_c, graphitization ratio from the manufactured pitch. Figure 2a, c, e shows that the amounts of boric acid increased, and d (002), d (004), and d (006) peaks related to crystallinity on the c-axis were blue-shifted and FWHM shows a decreasing tendency. This means that the graphitized crystal size increases. The d(002) value calculated via Bragg's equation ($\lambda = 2d\sin(\theta)$) is 3.374 Å and gradually decreases to 3.355 Å. This is close to the theoretical interlayer distance of graphite (3.353 Å). The calculated d(002) was used to calculate the graphitization ratio (= (3.44 − d(002)/(0.086)) [21]. The calculated graphitization ratio shows the highest value of 97.24% in 4203-B5-2500. The 4203-B1-2500 sample had a lower Lc than the 4203-B0-2500. This is in same to the previous results that the boron-doped graphite by substitution reaction shows a higher diffraction angle and shorter interlayer distance than that of non-boron-doped graphite. The variation of the interlayer spacing greatly depends on the competition between the weakened π-electron density and Poisson contraction effect, where the latter is responsible for the decrease in interlayer spacing. In our case at 4203-B1-2500, boron doping causes a increase in the π-electron density [28]. However, the decrease in Lc is interpreted as a result of the stacking structure not being able to develop. As the
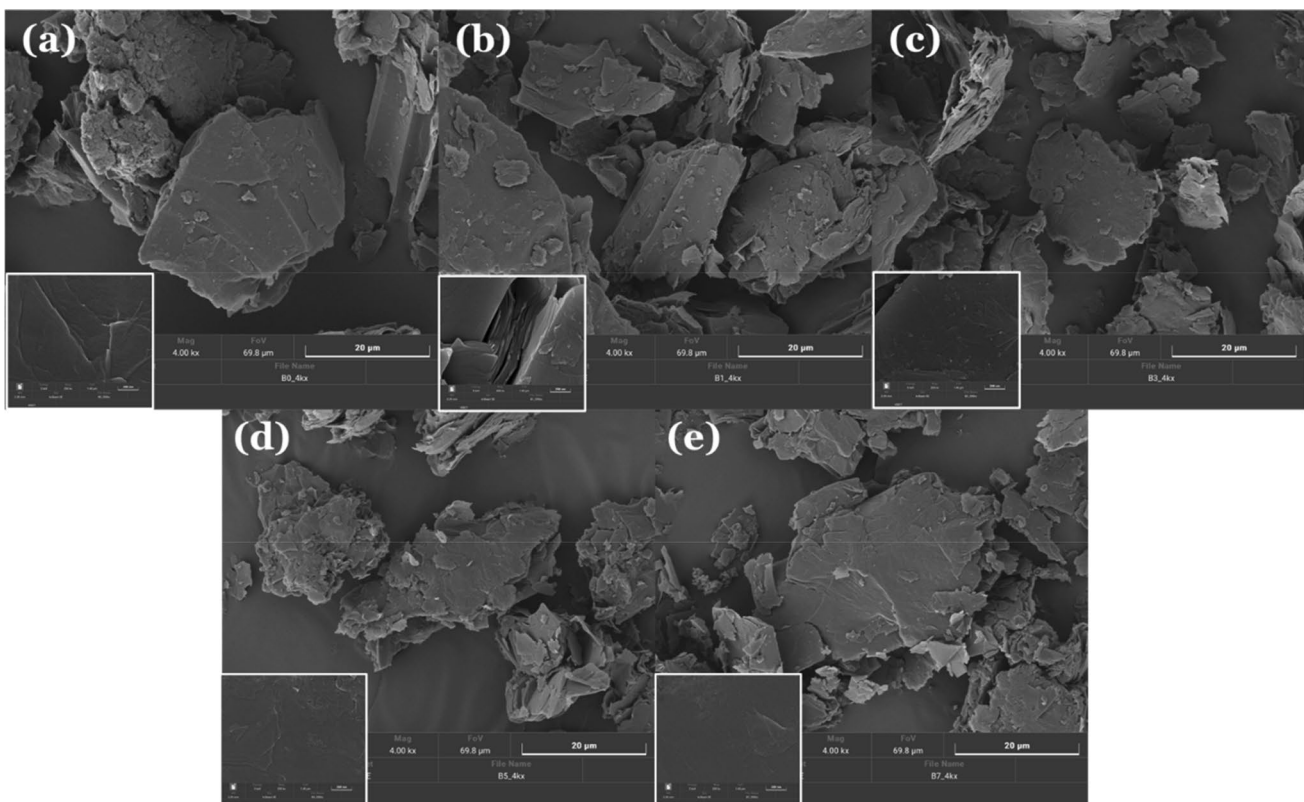
Fig. 2 SEM image of 4203-BX-2500 (×2000 magnification): **a** 4203-B0-2500, **b** 4203-B1-2500, **c** 4203-B3-2500, **d** 4203-B5-2500, **e** 4203-B7-2500. (The inserted image (bottom left) was measured at ×20,000 magnification.)
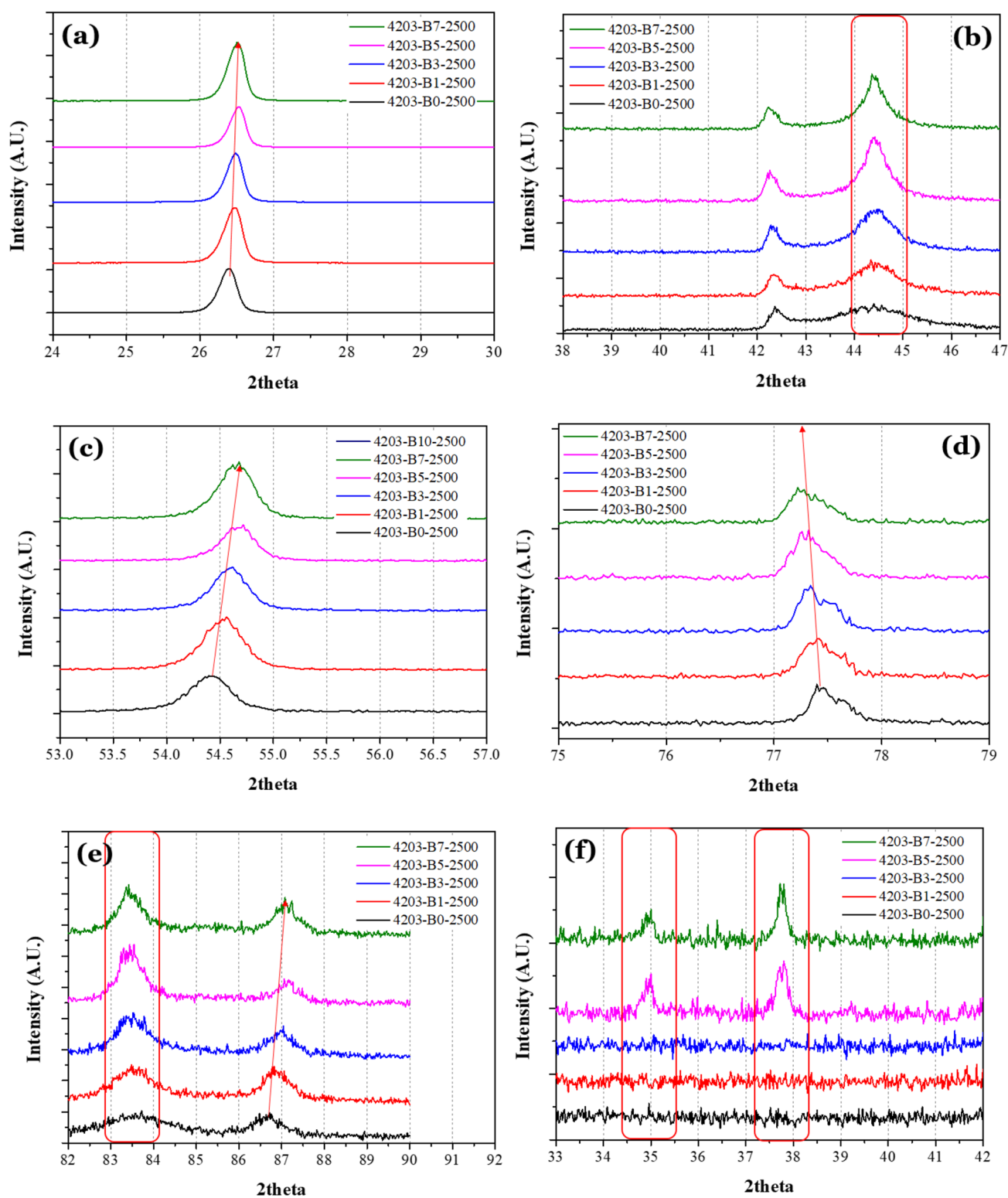
Fig. 3 X-ray diffraction patterns of 4203-BX-2500: **a** d(002), **b** d(100), d(101), **c** d(004), **d** d(110), **e** d(112), d(006), **f** B_4C

boric acid content increased, the result is similar to the general result. The decrease in d(002) with B-doping may be related to the depleted p-electrons between graphitic layers, which leads to a shorter interlayer distance, as well as to a lowering of the density of p-electrons within the graphite layers because of the lower valence state of
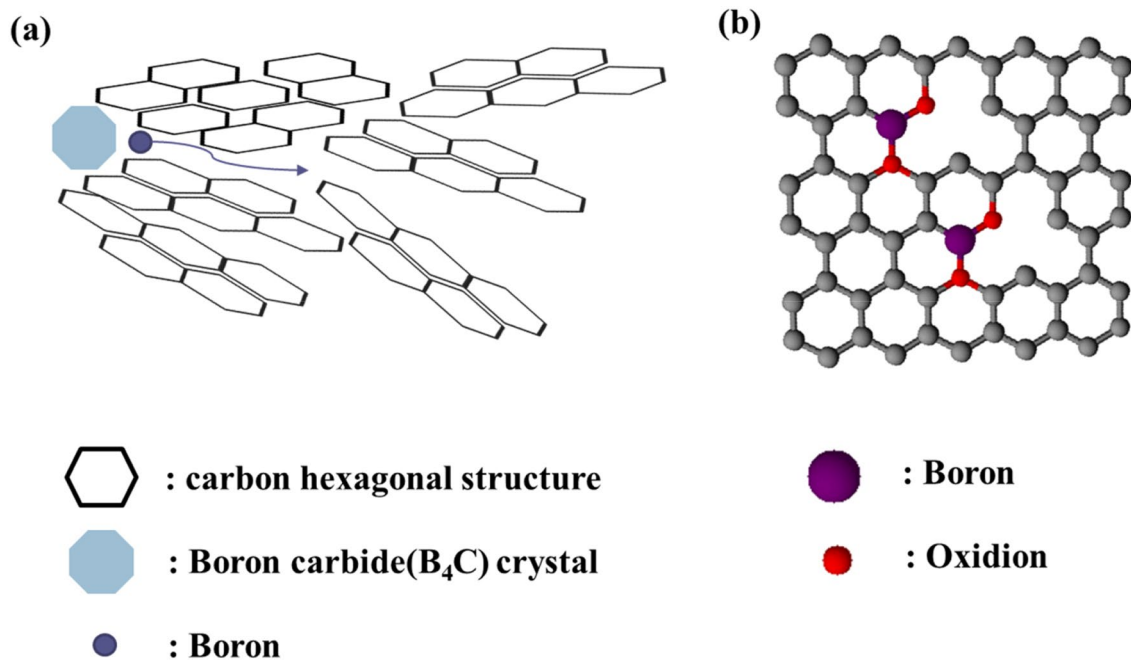
Fig. 4 Mechanism of 4203-BX-2500; **a** boron transfer by crystalline B_4C, **b** layer structure of 4203-BX-2500

Table 4 Calculated XRD value of 4203-BX-2500

	4203-B0-2500	4203-B1-2500	4203-B3-2500	4203-B5-2500	4203-B7-2500
002 peak (2θ)	26.3922	26.477	26.493	26.535	26.5164
100 peak (2θ)	42.40	42.33	42.36	42.24	42.32
d-spacing, 002 (Å)	3.374	3.36	3.36	3.356	3.358
d-spacing, 100 (Å)	2.1299	2.1334	2.1318	1.6777	1.6781
FWHM, 002	0.282	0.2936	0.2568	0.2444	0.267
FWHM, 100	0.32	0.288	0.281	0.324	0.351
La (Å)	544.18	604.50	619.63	537.17	495.99
Lc (Å)	286.02	274.77	314.15	330.12	302.17
Graphitization ratio (%)	76.5	88.83	91.16	97.24	94.54

boron relative to carbon [23]. However, the B_4C by heat treatment produced can interfere with graphitization. Therefore, a suitable boric acid content (less than 5 wt%) results in increased graphitization. However, excessively high boric acid content (7 wt%) is to inhibit graphitization by excessive B_4C formation. And this may also be mainly caused by the surface flaws etched by decomposition of B_2O_3 [29, 30]. It is considered that this is a reaction due to B_4C produced when synthetic graphite is synthesized by adding boric acid. According to Oya's work, boron vapor occurs at the contact point between the B_4C crystal and carbon particles, and the B_4C helps inject B into the carbon determining interior and is used as a additive to enhance graphitization (Fig. 4) [31]. Therefore, it is considered that high graphitization is exhibited from 5 wt% where B_4C is generated. However, excessively high boric acid content

(7 wt%) is to inhibit graphitization by excessive B_4C formation. Figure 3b, e shows (100) and (101) peaks and (112) and (006) peaks, respectively. These peaks are prominent in the carbon material containing 5 wt% or more of boron. The right shift of (002), (004), and (006) peaks can be interpreted as a result of improved crystallinity. In Fig. 2b–e, the peak related to the 3D structure ((101), (110), (112) peaks) moves to the left. This means that the ABAB stacking structure is developed [26]. In general, boron doping brings the adjacent planes closer and causes contraction of the structure along the c-axis [27]. The development of the stacking structure of graphite occurs by added boron. Structure development affects and decreases the lithium-ion intercalation resistance, which is thought to affect the battery characteristics such as the high-speed charge–discharge characteristics [14]. The L_c value calculated using

the Scherrer equation ($L_c = 0.89\lambda / \beta_c \cos(\theta_c)$) shows a maximum value of 330.12 Å for the 4203-B5-2500 sample and decreases thereafter. This is a process in which, as described in Ōya's work, the underlying mechanism is the passage of boron through the point of contact of the carbon particle with B_4C during the heating stage [32]. Therefore, it is considered that the crystallinity is increased (developed by turbostratic structure), and finally, the graphitic carbon structure is generated during the process of dissolving and reprecipitating B_4C particles at 2350 °C.

Figure 5 shows Raman spectroscopy results of the 4203-BX-2500 from the manufactured pitch. As the amount of boron added increases, the difference in intensity between the D and G peaks reduced, and the FWHM of each peak increases. In addition, the D' peak disappears due to an increase in the FWHM of the G peak. This change reflects an increase in the defect structure and a disordered graphite structure.

The changing I_D/I_G ratio is similar to the XRD crystallinity trend. When boric acid is added to 1 wt%, as the π-electron density decreased, stacking layers decreased and the intensity of G peak decreased. At the same time, doped boron increased the defect. As the amount of boron added increases, the crystallinity (c-axis) of carbon material having a graphite structure is increased, but the excessive boron accelerated the formation of small B_4C particles. In the process, the defects and disordered structure can be generated [32, 33].

An XPS analysis was conducted to identify the chemical bonds in the 4203-BX-2500 (Figs. 6, 7). The boron and oxygen atomic contents measured by XPS are 0, 0.4, 0.6, 1.2 and 1.7 at.% and 0.08, 0.10, 0.11, 4.5, 5.6 at.% in the order of boric acid content (0, 1, 3, 5, 7 wt%). The B1s peak was deconvoluted into three peaks at approximately 186,

187.3, and 193 eV. B–C bonding was analyzed at 186 eV in all samples. But as the content of boron increases, B_4C and B–O peaks are observed at 187.3 and 192.7 to 193 eV in addition to a B–C peak [34]. This was in agreement with the XRD analysis data. In addition, the XRD data for 4203-B3-2500 revealed unanalyzed B_4C peaks. This means that a boron compound (B_4C) is produced when the content of boric acid is 3 wt% or more [12, 19, 28, 32, 33, 35–37]. The C1s peak was deconvoluted into three peaks at approximately 284.5 (C–C sp^2), 285 (C–B), and 285.9–287 (C–C sp^3) eV. The C–C sp^3 defect in the 4203-B1-2500 sample is considered to have developed as a result of the low graphitization temperature. Also, the O1s peak was deconvoluted into two peaks at approximately 532.9 (B–C–O) and 533.6 (B–O) eV [34, 38, 39]. Further, it can be seen that the intensity of the peak of B–O is relatively strong from the 4203-B5-2500 and 4203-B7-2500 samples, which were judged to contain too much boric acid. The addition of excess boric acid is consistent with the Ōtani studies showing that boric acid can remain outside the graphite crystal [40]. Boron compound outside the crystal can act as an impurity in the process of recrystallization between graphite crystals, as described in the XRD data. In addition, for the 4203-B7-2500 sample a peak reflected BC_3 structure (189.1 eV) was observed [41, 42]. In this BC_3 structure, the binding length of B–C bonding was 1.562 Å and that of C–C bonding was 1.422 Å [41]. Therefore, when the hexagonal B–C structure inserts between the hexagonal C–C structures, defect can cause banding of graphene layer [27]. But the hexagonal B–C structures (BC_3 structures) exhibit higher electronic conductivity compared to other BC_2O and BCO_2 structures, which is approving for lithium-ion intercalation. It is considered that these defects can provide mobility of lithium ion and increase the high-speed charge/discharge
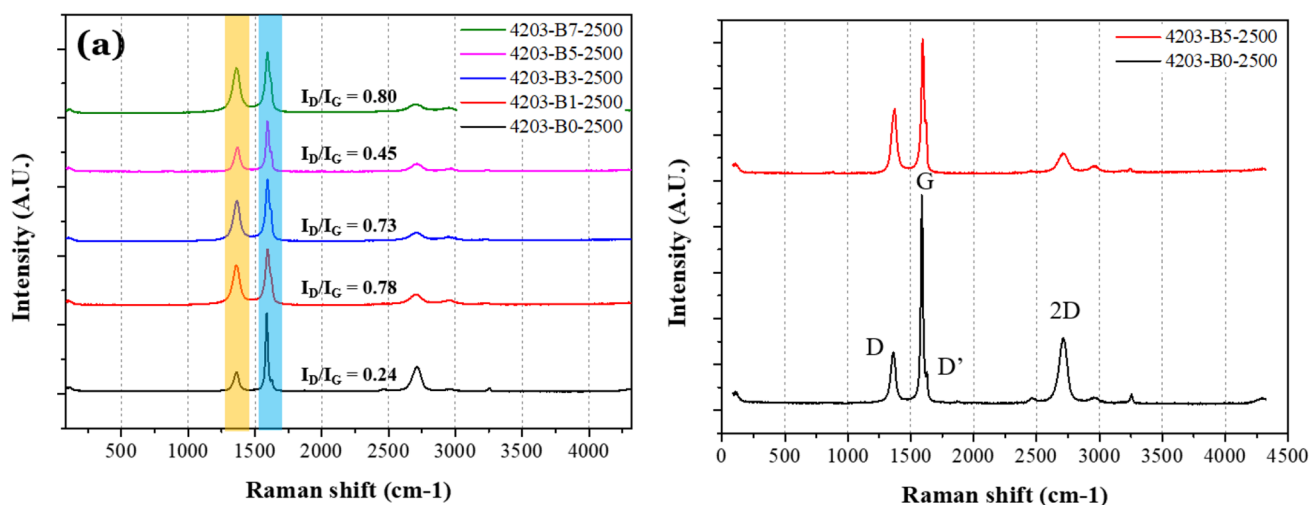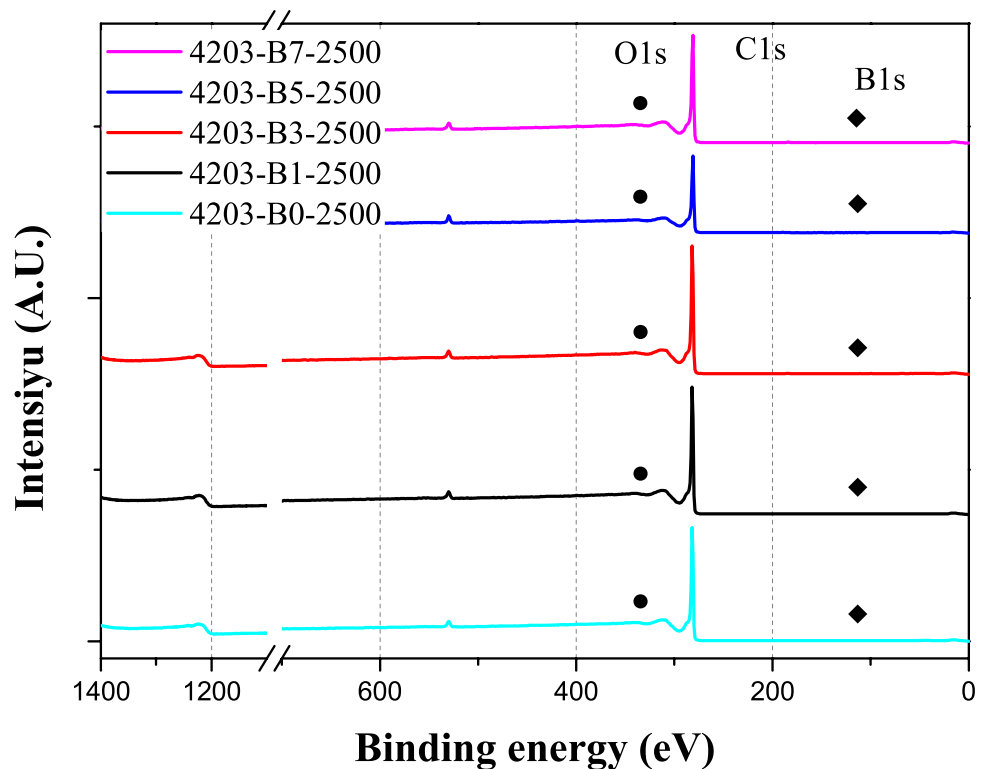

Fig. 5 Raman spectra of 4203-BX-2500

Fig. 6 XPS survey scan of 4203-BX-2500 and Fig. 7 shows detailed scan

characteristics. Experiments were conducted using a coin-type half-cell system to study the effects of the above structural characteristics on the charge–discharge and fast discharge properties.

3.3 Electrochemical performance of carbon materials produced from boric acid-added pitch

Figure 8 shows initial charge–discharge profiles and an initial charge capacity–initial coulombic efficiency graph of 4203-BX-2500 manufactured from a pitch according to the amount of boric acid added. Lithium insertion properties are shown in Fig. 8a, and it can be seen that as the amount of added boric acid increases, lithium insertion occurs earlier (red arrow). This is ascribed to the development of defects due to the addition of boron.

The insertion of lithium ions into a defect or pore of the carbon structure progresses via a mechanism involving storage in the cavity rather than through intercalation by staging between carbon layers at potentials of less than 0.25 V versus Li/Li$^+$ [43–46]. In general, storage of lithium ions in the pore and defects results in an increase in initial capacity (4203-B1-2500 → 4203-B3-2500), but the capacity decrease at (4203-B5-2500 → 4203-B7-2500) can be interpreted as a decrease in the specific capacity because an inactive metal (B_4C) is formed with respect to lithium ions [38, 47, 48].

Synthetic graphite produced by adding boric acid causes a defect in graphite hexagonal structure as shown in Fig. 4. In general, the surface defect of the anode material increases the reaction area with the electrolyte, which reduces the initial efficiency of the SEI layer of the first reaction. The addition of boric acid causes a defect due to boron doping and an increase in crystallinity due to the graphitization additive effect of boron. When the amount of boric acid is added at 1 wt%, doped boron can cause defect. And the amount of boric acid added increases, the increase in crystallinity becomes more noticeable. 4203-B7-2500 initial efficiency has higher than other samples, which is different from the tendency of structure analysis. This is associated with reduced charge capacity. The B_4C particles of 4203-B7-2500 reduced the insertion (discharge capacity) of lithium ions. and, B_4C causes a decrease in carbon structure alignment. As the carbon structure alignment decreases, more lithium can be de-intercalated (charge capacity).

Figures 9 and 10 are graphs of the discharge profile and the C-rate properties according to the different discharge (de-intercalation) rate of each manufactured sample. In the sample doped with boron in Fig. 8, a higher potential is measured when desorption of lithium ions starts at 2 C-rate. This means that desorption of lithium ions is not smooth. However, the content of boric acid increases and desorption of lithium ion begins at a lower potential. Yeo et. al. reported that rapid insertion and desorption of
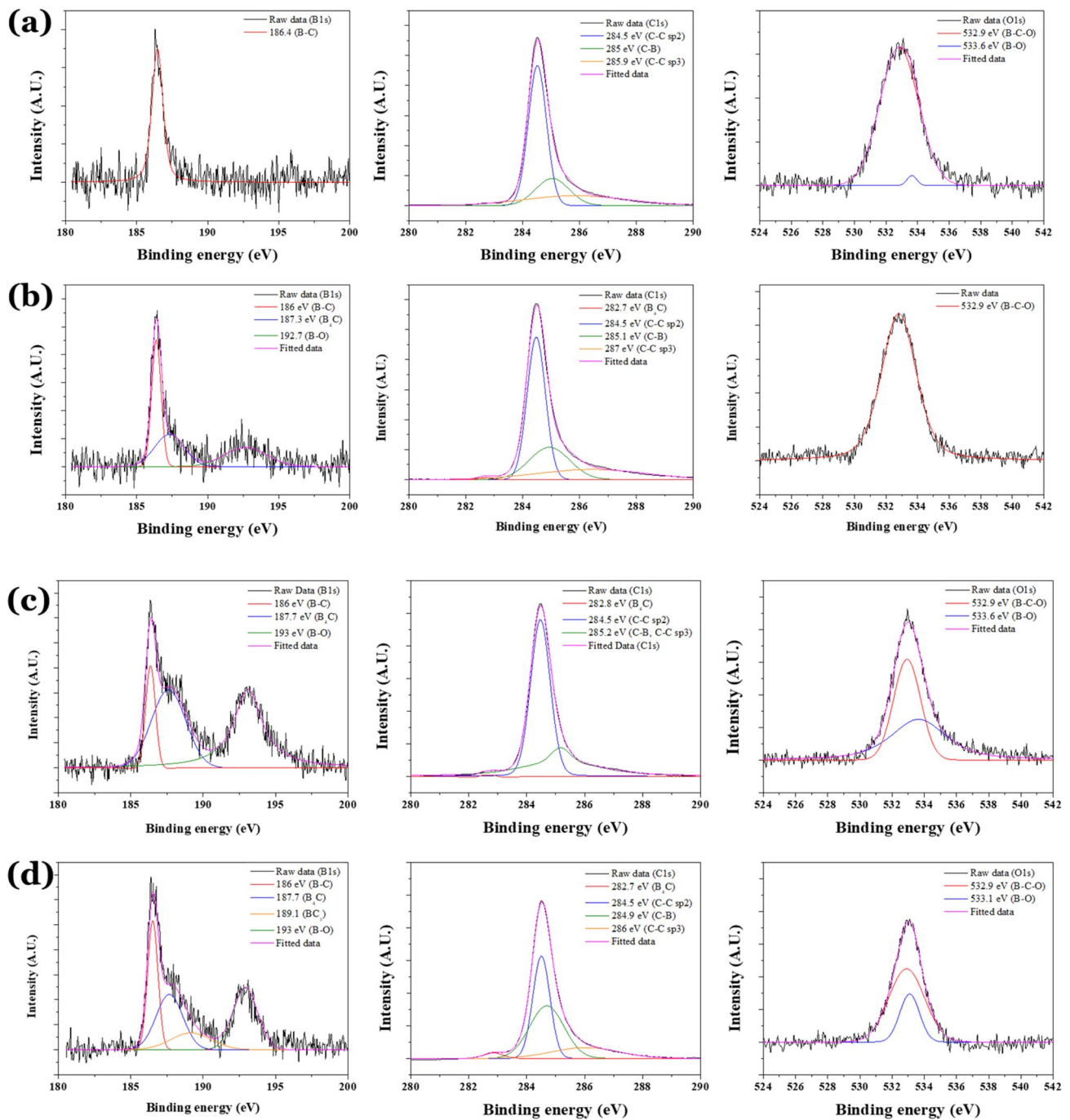
Fig. 7 XPS pattern of boron-doped SG: **a** 4203-B1-2500, **b** 4203-B3-2500, **c** 4203-B5-2500, and **d** 4203-B7-2500

lithium ions correlated with increased crystallinity and thus increased ion mobility [17]. Also, as seen in Fig. 9d, e, a small amount of lithium ions is desorbed at 0.9 V versus Li/Li$^+$ or higher (red boxes). These properties are observed with the addition of boron. It is considered that the boron functional group attached to the carbon edge site reacts with lithium ions to act on the capacity [49]. Figure 10 shows the C-rate performance and cycle retention

performance of each anode material. The 4203-B0-2500 to 4203-B7-2500 samples have C-rate performance of 92.4, 93.1, 91.4, 94.5, and 94.7% and cycle retention performance of 97.1, 99.7, 98.7, 96.7 and 100.1%, respectively. The C-rate performance of the sample containing 5 wt% or more of boric acid was the highest. However, the cycle retention test did not show a significant difference between the anode materials. When B$_4$C was produced,
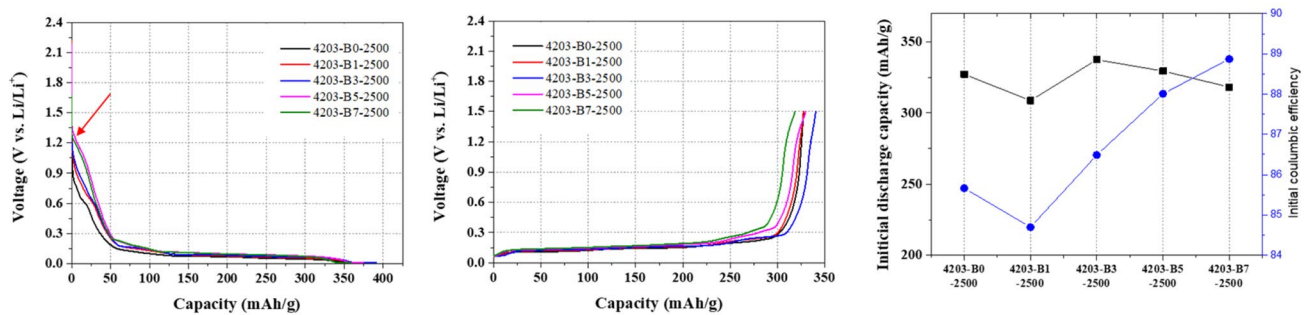
Fig. 8 Initial charge–discharge profile and coulombic efficiency of 4203-BX-2500
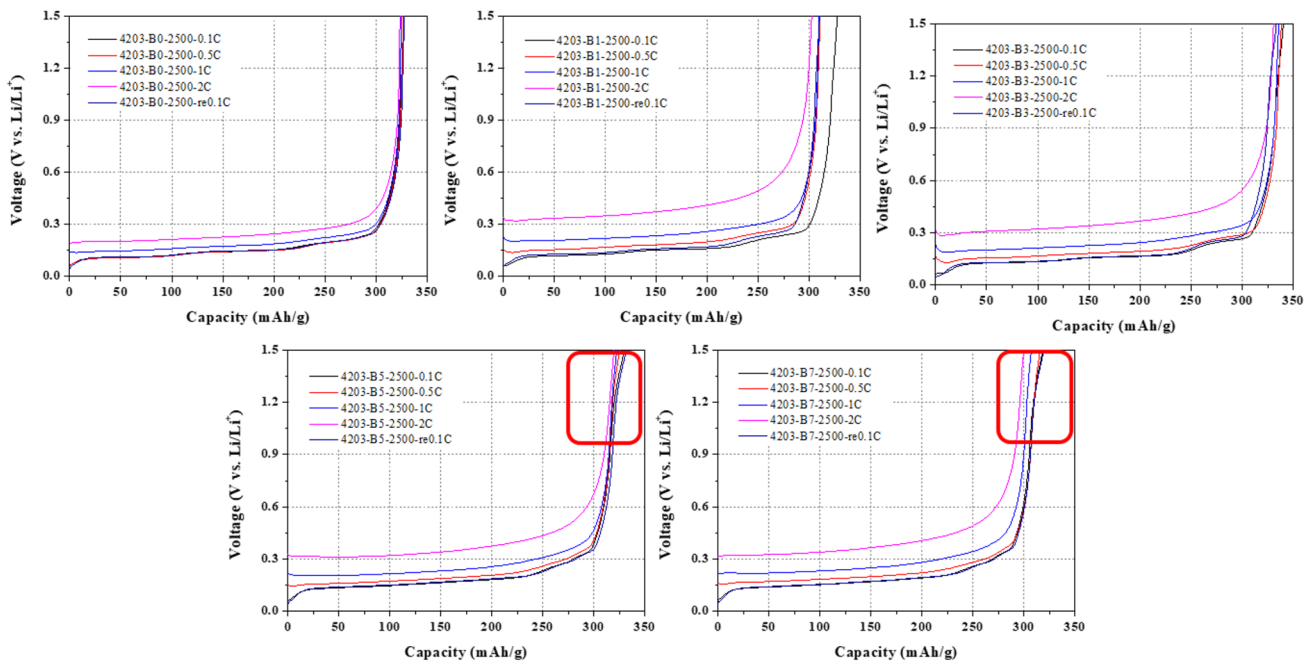
Fig. 9 Discharge profile of C-rate performance of 4203-BX-2500

the three-dimensional disordered structure was produced. The three-dimensional structure acts as resistance when lithium ions move, but paradoxically, it is considered that the addition of boron improved the velocity characteristics due to the developed interlayer structure and the defects of the graphene layer [50, 51].

Figure 11 shows the dQ/dV graph for analyzing the electrochemical reaction at the first and second cycles. The position of each peak indicates the electrochemical reaction at that potential, and the size of the peak indicates the reactivity. When compared with the first cycle in all graphs, the reaction due to the intercalation of lithium ions is clearly observed in the second cycle. In particular, in the sample showing high graphitization without the formation of B_4C (Fig. 10c, 4203-B3-2500), sharp peaks can be observed at 0.1, 0.13, and 0.22 V versus Li/Li$^+$ of the charge

graph in the second cycle. Each peak serves as a standard for separating the stages from the lithium ion insertion mechanism. Therefore, the higher the peak intensity and the lower the FWHM are, the higher the migration of lithium ions is, due to the lower electrode resistance [18]. However, in the graphs (Fig. 10d, e) of the samples where a high graphitization ratio was measured, a broad and low peak is shown, which is the three-dimensional shape described in the XRD and XPS results. This is likely due to the defects on the carbon surface. Nonetheless, the graph showed the highest graphitization. Figure 11d, e shows broad and low peaks, likely due to the three-dimensional structure described in the XRD and XPS results and the defect described in the Raman results. In general, the peak is clearly measured in the dQ/dV graph of the anode material with the developed graphite structure. However, in the
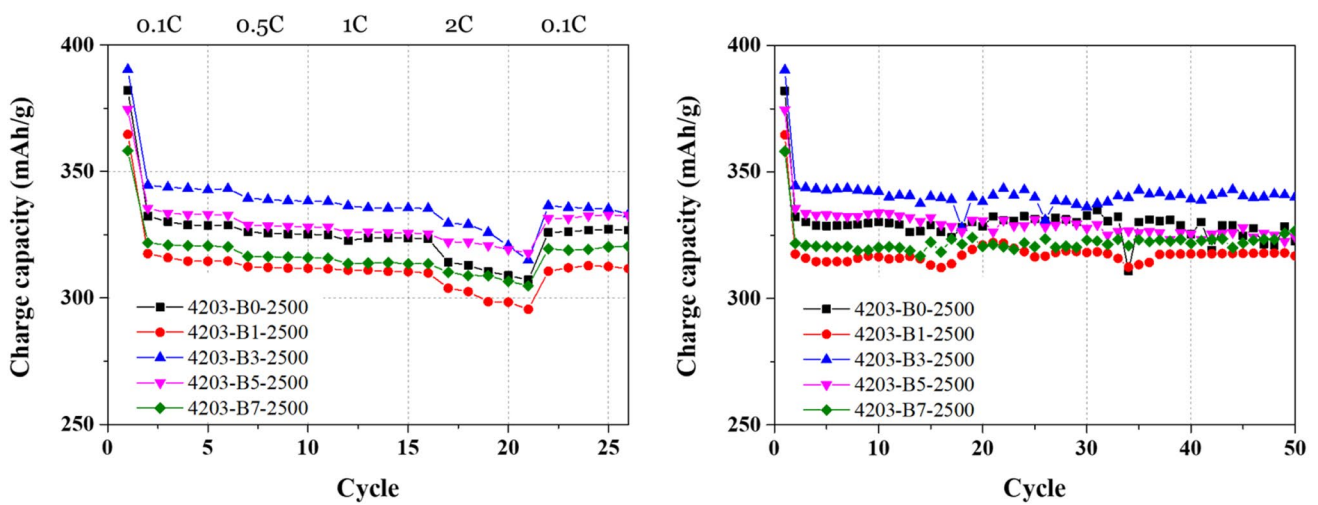
Fig. 10 C-rate performance and cycle retention performance of 4203-BX-2500
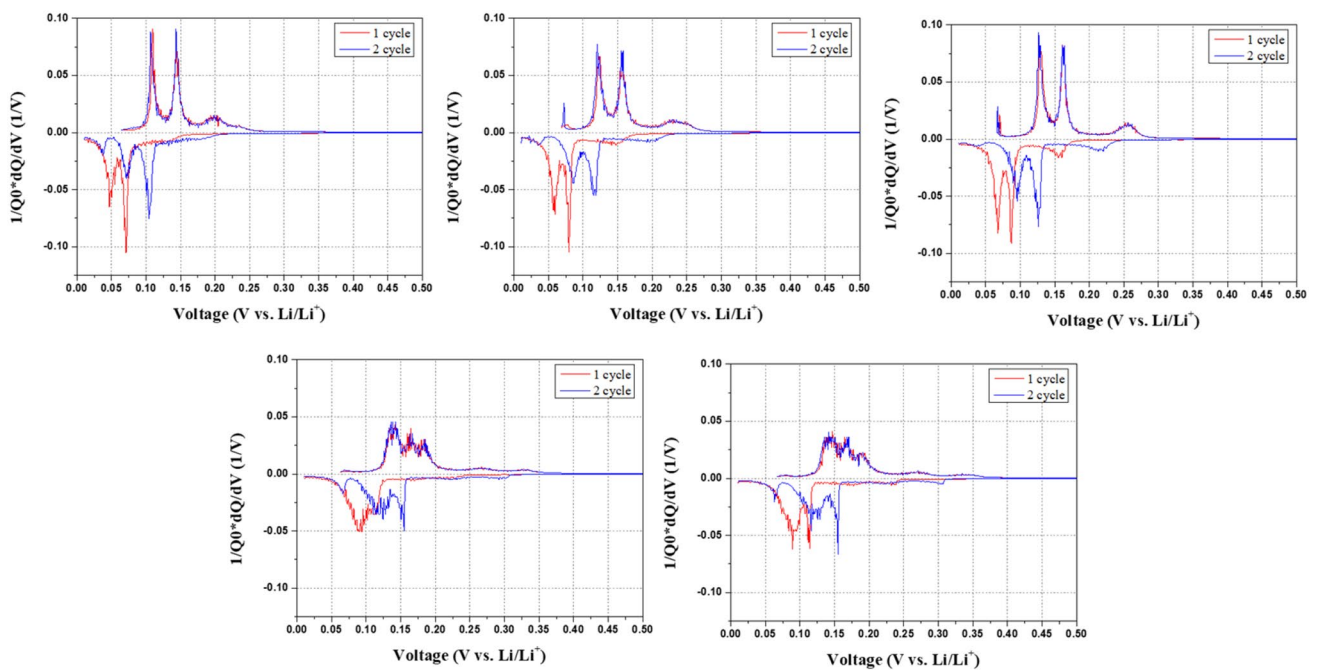

Fig. 11 Differential of first and second cycle profiles. **a** 4203-B0-2500, **b** 4203-B1-2500, **c** 4203-B3-2500, **d** 4203-B5-2500, **e** 4203-B7-2500

material in this study with a large amount of boron added, lithium ions not only undergo intercalation/de-intercalation in the edge plane but are also formed by defects in the graphene layer and are observed as broad peaks [18].

According to the research result of Yang et al., when a defect occurs in the graphene layer, the electrical conductivity decreases. However, when calculating the lithium ion diffusion energy in the graphene layer, low diffusion energy was measured in the path through

which lithium ions were transferred using the edge of the defect. Thus, 4203-B1-2500–4203-B7-2500 has a higher speed discharge characteristic than 4203-B0-2500. Also, the defect acts as a passage for lithium ions to move between the layers and is expected to have high high-speed lithium insertion efficiency. However, if too many defects caused the structural stability can rather be reduced [52].

4 Conclusion

In this paper, pitch was prepared from boric acid and PFO, and then, it is used to make the cokes and SG, and the physical and electrochemical properties were analyzed using XRD, Raman, charge–discharge test, fast discharge test. As a result of producing 4203-BX-2500 by changing the amount of added boric acid, the crystallinity of SG increased as the content of boric acid increased, but B_4C and C–C sp^3 structures as by-products were obtained. The by-product is irreversible to the electrochemical reaction, and thus, it can reduce the capacity of the battery and act as resistance during the internal migration of lithium ions. However, nevertheless, a high graphitization ratio and high C-rate performance results could be obtained. However, if the above-mentioned by-products can be controlled, it will be possible to manufacture an anode material having better physical and electrochemical properties.

Declarations

Conflict of interest The authors declare that they have no competing interests

References

1. Endo K, Zhang HP, Fu LJ, Lee KJ, Sekine K, Takamura T, Jeong YU, Wu YP, Holze R, Wu HQ (2006) Electrochemical performance of a novel surface modified spherical graphite as anode material for lithium ion batteries. J Appl Electrochem 36(11):1307–1310
2. Ambrosi A, Chua CK, Khezri B, Sofer Z, Webster RD, Pumera M (2012) Chemically reduced graphene contains inherent metallic impurities present in parent natural and synthetic graphite. Proc Natl Acad Sci 109(32):12899–12904
3. Shi H, Barker J, Saidi MY, Koksbang R (1996) Structure and lithium intercalation properties of synthetic and natural graphite. J Electrochem Soc 143(11):3466
4. Wang C, Zhao H, Wang J, Wang J, Lv P (2013) Electrochemical performance of modified artificial graphite as anode material for lithium ion batteries. Ionics 19(2):221–226
5. Xing B, Zhang C, Cao Y, Huang G, Liu Q, Zhang C, Chen Z, Yi G, Chen LB, Yu J (2018) Preparation of synthetic graphite from bituminous coal as anode materials for high performance lithium-ion batteries. Fuel Process Technol 172:162–171
6. Dong S, Alvarez P, Paterson N, Dugwell DR, Kandiyoti R (2009) Study on the effect of heat treatment and gasification on the carbon structure of coal chars and metallurgical cokes using Fourier transform Raman spectroscopy. Energy Fuels 23(3):1651–1661
7. Lascovich JC, Giorgi R, Scaglione S (1991) Evaluation of the sp^2/sp^3 ratio in amorphous carbon structure by XPS and XAES. Appl Surf Sci 47(1):17–21
8. Franklin RE (1951) Crystallite growth in graphitizing and non-graphitizing carbons. Proc R Soc Lond A 209(1097):196–218
9. Winter M, Besenhard JO, Spahr ME, Novak P (1998) Insertion electrode materials for rechargeable lithium batteries. Adv Mater 10(10):725–763
10. Dahn JR, Zheng T, Liu Y, Xue JS (1995) Mechanisms for lithium insertion in carbonaceous materials. Science 270(5236):590–593
11. Wang J, Liu JL, Wang YG, Wang CX, Xia YY (2012) Pitch modified hard carbons as negative materials for lithium-ion batteries. Electrochim Acta 74:1–7
12. Zhou X, Ma L, Yang J, Huang B, Zou Y, Tang J, Xie J, Wang S, Chen G (2013) Properties of graphitized boron-doped coal-based coke powders as anode for lithium-ion batteries. J Electroanal Chem 698:39–44
13. Fujimoto H, Mabuchi A, Natarajan C, Kasuh T (2002) Properties of graphite prepared from boron-doped pitch as an anode for a rechargeable Li ion battery. Carbon 40(4):567–574
14. Ding S, Zheng S, Xie M, Peng L, Guo X, Ding W (2011) One-pot synthesis of boron-doped mesoporous carbon with boric acid as a multifunction reagent. Microporous Mesoporous Mater 142(2–3):609–613
15. Kim JG, Liu F, Lee CW, Lee YS, Im JS (2014) Boron-doped carbon prepared from PFO as a lithium-ion battery anode. Solid State Sci 34:38–42
16. Jung JY, Park MS, Kim MI, Lee YS (2014) Novel reforming of pyrolyzed fuel oil by electron beam radiation for pitch production. Carbon Lett 15(4):262–267
17. Wu X, Radovic LR (2005) Inhibition of catalytic oxidation of carbon/carbon composites by boron-doping. Carbon 43(8):1768–1777
18. Rodriguez E, Camean I, García R, García AB (2011) Graphitized boron-doped carbon foams: performance as anodes in lithium-ion batteries. Electrochim Acta 56(14):5090–5094
19. Yeo JS, Park TH, Seo MH, Miyawaki J, Mochida I, Yoon SH (2013) Enhancement of the rate capability of graphite via the introduction of boron-oxygen functional groups. Int J Electrochem Sci 8(1):1308–1315
20. Burgess JS, Acharya CK, Lizarazo J, Yancey N, Flowers B, Kwon G, Klein T, Weaver M, Lane AM, Turner CH, Street S (2008) Boron-doped carbon powders formed at 1000 °C and one atmosphere. Carbon 46(13):1711–1717
21. Murty HN, Biederman DL, Heintz EA (1977) Apparent catalysis of graphitization. 3. Effect of boron. Fuel 56(3):305–312
22. Liu T, Luo R, Yoon SH, Mochida I (2010) Anode performance of boron-doped graphites prepared from shot and sponge cokes. J Power Sources 195(6):1714–1719
23. Endo M, Kim C, Karaki T, Nishimura Y, Matthews MJ, Brown SDM, Dresselhaus MS (1999) Anode performance of a Li ion battery

based on graphitized and B-doped milled mesophase pitch-based carbon fibers. Carbon 37(4):561–568

24. Ishii T, Kaburagi Y, Yoshida A, Hishiyama Y, Oka H, Setoyama N, Ozaki JI, Kyotani T (2017) Analyses of trace amounts of edge sites in natural graphite, synthetic graphite and high-temperature treated coke for the understanding of their carbon molecular structures. Carbon 125:146–155

25. Yin G, Gao Y, Shi P, Cheng X, Aramata A (2003) The effect of boron doping on lithium intercalation performance of boron-doped carbon materials. Mater Chem Phys 80(1):94–101

26. Jurkiewicz K, Pawlyta M, Burian A (2018) Structure of carbon materials explored by local transmission electron microscopy and global powder diffraction probes. J Carbon Res 4(4):68

27. Endo M, Kim C, Karaki T, Tamaki T, Nishimura Y, Matthews MJ, Brown SDM, Dresselhaus MS (1998) Structural analysis of the B-doped mesophase pitch-based graphite fibers by Raman spectroscopy. Phys Rev B 58(14):8991

28. Wang G, Li X, Wang Y, Zheng Z, Dai Z, Qi X, Liu L, Cheng Z, Xu Z, Tan PH, Zhang Z (2017) Interlayer coupling behaviors of boron doped multilayer graphene. J Phys Chem C 121(46):26034–26043

29. Jung CH, Lee MJ, Kim CJ (2004) Preparation of carbon-free B_4C powder from B_2O_3 oxide by carbothermal reduction process. Mater Lett 58(5):609–614

30. Wen Y, Lu Y, Xiao H, Qin X (2012) Further investigation on boric acid catalytic graphitization of polyacrylonitrile carbon fibers: mechanism and mechanical properties. Mater Des (1980–2015) 36:728–734

31. Slutskii VG, Severin ES, Polenov LA (2007) An Ab initio study of reactions in the $H_3BO_3/B_2O_3/H_2O$ system. Russ J Phys Chem B 1(6):549–552

32. Robson HE, Gilles PW (1964) The high temperature vaporization properties of boron carbide and the heat of sublimation of boron1. J Phys Chem 68(5):983–989

33. Tai FC, Wei C, Chang SH, Chen WS (2010) Raman and X-ray diffraction analysis on unburned carbon powder refined from fly ash. J Raman Spectrosc 41(9):933–937

34. Wu T, Shen H, Sun L, Cheng B, Liu B, Shen J (2012) Nitrogen and boron doped monolayer graphene by chemical vapor deposition using polystyrene, urea and boric acid. New J Chem 36(6):1385

35. Ōya A, Yamashita R, Ōtani S (1979) Catalytic graphitization of carbons by borons. Fuel 58(7):495–500

36. Kim YA, Fujisawa K, Muramatsu H, Hayashi T, Endo M, Fujimori T, Kaneko K, Terrones M, Behrends J, Eckmann A, Casiraghi C, Novoselov KS, Saito R, Casiraghi C (2012) Raman spectroscopy of boron-doped single-layer graphene. ACS Nano 6(7):6293–6300

37. Cattelan M, Agnoli S, Favaro M, Garoli D, Romanato F, Meneghetti M, Barinov A, Dudin P, Granozzi G (2013) Microscopic view on a chemical vapor deposition route to boron-doped graphene nanostructures. Chem Mater 25(9):1490–1495

38. Mishra A, Rakesh KS, Saroj KS, Mishra KB (2018) Synthesis of low carbon boron carbide powder using a minimal time processing route: thermal plasma. J Asian Ceram Soc 3(4):373–376

39. Thirumal V, Pandurangan A, Jayavel R, Ilangovan R (2016) Synthesis and characterization of boron doped graphene nanosheets for supercapacitor applications. Synth Metals 220:524–532

40. Ōya A, Ōtani S (1979) Catalytic graphitization of carbons by various metals. Carbon 17(2):131–137

41. Van Tam T, Kang SG, Babu KF, Oh E-S, Lee SG, Choi WM (2017) Synthesis of B-doped graphene quantum dots as a metal-free electrocatalyst for the oxygen reduction reaction. J Mater Chem A 5(21):10537–10543

42. Endo M, Hayashi T, Hong S-H, Enoki T, Dresselhaus MS (2001) Scanning tunneling microscope study of boron-doped highly oriented pyrolytic graphite. J Appl Phys 90(11):5670–5674

43. Blyth RIR, Buqa H, Netzer FP, Ramsey MG, Besenhard JO, Golob P, Winter M (2000) XPS studies of graphite electrode materials for lithium ion batteries. Appl Surf Sci 167(1–2):99–106

44. Vu DL, Kwon YJ, Lee SC, Lee JU, Lee JW (2019) Exfoliated graphene nanosheets as high-power anodes for lithium-ion batteries. Carbon Lett 29(1):81–87

45. Flandrois S, Simon B (1999) Carbon materials for lithium-ion rechargeable batteries. Carbon 37(2):165–180

46. Mabuchi A, Tokumitsu K, Fujimoto H, Kasuh T (1995) Charge-discharge characteristics of the mesocarbon miocrobeads heat-treated at different temperatures. J Electrochem Soc 142(4):1041

47. Shaker M, Ghazvini AAS, Qureshi FR, Riahifar R (2021) A criterion combined of bulk and surface lithium storage to predict the capacity of porous carbon lithium-ion battery anodes: lithium-ion battery anode capacity prediction. Carbon Lett 1–6

48. Lee SE, Kim JH, Lee YS, Bai BC, Im JS (2020) Effect of crystallinity and particle size on coke-based anode for lithium ion batteries. Carbon Lett 1–10

49. Tanaka U, Sogabe T, Sakagoshi H, Ito M, Tojo T (2001) Anode property of boron-doped graphite materials for rechargeable lithium-ion batteries. Carbon 39(6):931–936

50. Fromm O, Heckmann A, Rodehorst UC, Frerichs J, Becker D, Winter M, Placke T (2018) Carbons from biomass precursors as anode materials for lithium ion batteries: new insights into carbonization and graphitization behavior and into their correlation to electrochemical performance. Carbon 128:147–163

51. Sonia FJ, Jangid MK, Ananthoju B, Aslam M, Johari P, Mukhopadhyay A (2017) Understanding the Li-storage in few layers graphene with respect to bulk graphite: experimental, analytical and computational study. J Mater Chem A 5(18):8662–8679

52. Yang C, Zhang X, Li J, Ma J, Xu L, Yang J, Liu S, Fang S, Li Y, Sun X, Yang X, Pan F, Lu J, Yu D (2020) Holey graphite: a promising anode material with ultrahigh storage for lithium-ion battery. Electrochimica Acta 346:136244